Numerical investigation on the effect of transversal fluid field deformation on heat transfer in a rod bundle with mixing vanes

Tas-Köhler, S.; Lecrivain, G.; Krepper, E.; Unger, S.; Hampel, U.;

Originally published:

February 2020

Nuclear Engineering and Design 361(2020), 110575

DOI: https://doi.org/10.1016/j.nucengdes.2020.110575

Numerical investigation on the effect of transversal fluid field deformation on heat transfer in a rod bundle with mixing vanes

Sibel Tas-Koehler [a,b]*, Gregory Lecrivain [a], Eckhard Krepper [a], Sebastian Unger [a], Uwe Hampel [a,c]

[a] Helmholtz-Zentrum Dresden-Rossendorf, Institute of Fluid Dynamics, Bautzner Landstr. 400, 01328 Dresden, Germany

[b] Middle East Technical University, Department of Mechanical Engineering, Dumlupınar Blv. No: 1, 06800 Ankara, Turkey

[c] Technische Universität Dresden, Chair of Imaging Techniques in Energy and Process Engineering, 01062 Dresden, Germany

* CORRESPONDING AUTHOR (E-MAIL: s.tas@hzdr.de)

ABSTRACT

Spacer grids of fuel rod assemblies are equipped with vanes, which promote flow mixing and turbulence within and across the sub-channels, thereby enhancing the heat transfer. First, a literature study about the various effect of the spacer grid has on the sub-channel thermo-hydrodynamics is provided. It follows, that the multiple effects on the vane angle are insufficiently understood. The effect of the vane angle on design parameters, namely the evolution of the Nusselt number, the pressure drop, the cross and swirl flows, is here further discussed and supplemented by own simulations. The effect of the velocity gradient tensor $\nabla \otimes \boldsymbol{u}$, decomposed into a strain and a vorticity contribution, is also looked at downstream of the spacer grid. The RNG k-ε turbulence model was found to provide results best matching the experimental data available in the literature. The use of vanes results in the formation of a downstream vortex. As the flow develops downstream of the spacer grid, the vortex migrates away from the sub-channel center and eventually weakens. In line with the presented literature survey, it is confirmed that a vane angle of about 30° provides optimal swirl and cross flows, resulting in an enhanced heat transfer.

Keywords: Literature analysis, Vortex generator, Vane angle, Rod bundle, Vorticity, Turbulent flow, Heat transfer.

Nomenclature

Latin symbols

c_p	specific heat [J kg^{-1} K^{-1}]
D	rod diameter [m]
D_h	hydraulic diameter [m]
g	coordinate in G direction [m]
G	minimum distance between the rod surfaces [m]
L	axial length [m]
L_e	entrance length [m]
l_{spacer}	spacer grid length [mm]
h	heat transfer coefficient [W m^{-2} K^{-1}]
k	turbulent kinetic energy [m^2 s^{-2}]
Nu	Nusselt number [-]
Re	Reynolds number [-]
P	rod pitch [m], pressure [Pa], turbulent energy production [kg m^{-1} s^{-3}]
r	radial distance from the centre of the sub-channel [m]
R	effective swirl radius [m]
S_{ij}	rate-of-strain tensor [s^{-1}]
q	wall heat flux [W m^{-2}]
T, T_b, T_w	temperature, bulk temperature, wall temperature [K]
U	mean flow velocity [m s^{-1}]
U_a	local axial velocity [m s^{-1}]
U_b	axial velocity averaged over a cross-sectional plane [m s^{-1}]
U_{lat}	lateral velocity [m s^{-1}]
U_{tan}	tangential mean velocity [m s^{-1}]
u'	time-averaged fluctuating velocity [m s^{-1}]
u,v,w	velocity in x, y, z [m s^{-1}]
W	vane base length [m]
t	time [s]

Greek symbols

λ	thermal conductivity [W m^{-1} K^{-1}]
ρ	density [kg m^{-3}]
ε	turbulence dissipation rate [m^2 s^{-3}]
μ	dynamic viscosity [kg m^{-1} s^{-1}]
μ_t	turbulent viscosity [kg m^{-1} s^{-1}]
$\emptyset$	viscous dissipation function [s^{-2}]
ω	vorticity [s^{-1}], turbulence frequency [s^{-1}]
Ω_{ij}	rate-of-rotation tensor [s^{-1}]
τ_{ij}	stress tensor [kg m^{-1} s^{-2}]
δ_{ij}.	Kroenecker delta function
α	vane angle [°]

Acronyms

CFD: computational fluid dynamics
CHF: critical heat flux
LDA: Laser Doppler anemometry
LDV: Laser Doppler velocimetry
LSVF: large scale vortex flow
RMS: root mean square
RNG: re-normalization group
RSM: Reynolds stress model
SAS: scale-adaptive simulation
SSG: Speziale-Sarkar-Gatski
SST: shear stress transport
TKE: turbulent kinetic energy
TVSG: twist vane spacer grid

1. Introduction

In a nuclear reactor, the fission heat must be efficiently removed from the surface of the fuel rods by the coolant fluid. In the event of critical heat flux (CHF), the formation of a local film boiling with low heat transfer may potentially lead to cladding damages. A preventing measure to counteract this risk is to support the fuel rods with spacer grids equipped with vanes generating swirl and cross flows. These vanes (or vortex generators) promote both the near-wall turbulence and the enthalpy exchange between the sub-channels. Measuring the local flow and the heat transfer is, however, experimentally difficult. Thus, there has been a continuous interest in employing Computational Fluid Dynamics (CFD) simulations. The following section provides a brief, yet detailed, state-of-the-art summary on the recent numerical and experimental studies in the field.

Hereafter, the Reynolds number (Re) is defined with the mean velocity inlet (U), the hydrodynamic diameter of the sub-channel cross-section (D_h), and the kinematic viscosity of the coolant fluid (η). The hydrodynamic diameter (D_h) is defined with the rod diameter (D) and the rod pitch (P). The Nusselt number (Nu) is defined with the thermal conductivity of the rod material (λ) and the heat transfer coefficient (h). This latter (h) is defined with the applied heat flux (q), the bulk temperature (T_b), and the wall temperature (T_w). The Reynolds number, the hydraulic diameter, the Nusselt number, and the heat transfer coefficient are given by

$$Re = \frac{U\,D_h}{\eta}, \quad (1)$$

$$D_h = \mathrm{D}\left[\frac{4}{\pi}\left(\frac{P}{D}\right)^2 - 1\right], \quad (2)$$

$$Nu = \frac{h\,D_h}{\lambda}, \quad (3)$$

$$h = \frac{q}{T_b - T_w}. \quad (4)$$

Besides, the swirl flow factor (S_r) and the cross-flow factor (C_r) are defined as

$$S_\mathrm{r} = \frac{1}{\mathrm{R}} \int \frac{U_\mathrm{tan}}{U_a}\,\mathrm{dr}, \quad (5)$$

$$C_\mathrm{r} = \frac{1}{\mathrm{G}} \int \frac{|U_\mathrm{lat}|}{U_b}\,\mathrm{dg}, \quad (6)$$

with the tangential mean flow velocity component (U_tan), the local axial component (U_a), the radial distance from the centre of the sub-channel (r), the effective swirl radius (R), the lateral velocity component (U_lat) perpendicular to the axial direction (g), the axial velocity averaged over a cross-sectional plane (U_b), and the minimum distance between the rod surfaces (G). The length (L) is also defined as the axial distance from the vane tips.

1.1 Flow hydrodynamics downstream of the spacer grid

The flow hydrodynamics have been studied for various types of vanes and vane angles. Table 1 and Table 2 present a list of recent experimental and numerical works respectively dealing with the flow dynamics downstream of a spacer grid.

Researchers	Laboratory condition	Type of spacer grid	Aim of the study
Chang *et al.* (2008) [1]	Laser Doppler Anemometry (LDA) 5x5 rod bundle $Re = 50{,}000$	Split vane (30 Swirl vane (35°)	Analysis of turbulent flow mixing in a rod bundle
Chang *et al.* (2014) [2]	LDA 5x5 rod bundle $Re = 48{,}000$	Split vane Swirl vane	Investigation of turbulent flow structures
Wang *et al.* (2016) [3]	Laser induced fluorescence (LIF) 3x3 rod bundle $Re = 2010$	Split type	Analysis of and visualization of the fluid mixing process in a rod bundle
Shen *et al.* (1991) [4]	LDV 4x4 rod bundle $Re = 14{,}200$	Mixing blades (0°, 20°, 25°, 30° ,35°)	Distributions of transverse mean velocity and RMS velocity
Holloway *et al.* (2008) [5]	Temperature measurements 5x5 rod bundle $Re = 29{,}000 - 35{,}000$	Standard grid Split vane (30°) Disc vane	Investigation of convection-induced heat transfer
Byun *et al.* (2018) [6]	LDV 6x6 rod bundle $Re = 30{,}000 - 50{,}000$	Split type Large scale vortex flow type (30°)	Heat transfer characteristics for downstream flow in the support grid
In *et al.* (2015) [7]	Temperature measurements 3x3 rod bundle $Re = 42{,}000$	Twisted vane (35°)	Investigation of the convective heat transfer enhancement in a rod bundle by twist-vane spacer grid.
Moon *et al.* (2014) [8]	Temperature measurements 6x6 rod bundle $Re = 1121 - 13{,}600$	Split vane	Heat transfer enhancement by spacer grids in single-phase steam flow
Han *et al.* (2009) [9]	LDA 6x6 rod bundle $Re = 50{,}000$	Tandem arrangement vanes (30°)	Investigation the thermal hydraulic flow characteristics in sub-channels
Caraghiaur *et al.* (2009) [10]	LDV 24 fuel rod bundle $Re = 10{,}000 - 50{,}000$	Standard grid	Investigation of the phenomena that govern turbulent flows in fuel rod assemblies with spacers
Ikeda (2014) [11]	Laser Doppler velocimetry (LDV) 5x5 rod bundle $Re = 40{,}000 - 50{,}000$	Split vane (30°)	Investigation the local velocity profile in a rod bundle and inside a spacer grid.
McClusky *et al.* (2003) [12]	Particle image velocimetry (PIV) 5x5 rod bundle $Re = 28{,}000$	Split vane (30°)	Investigation of lateral flow
Xiong *et al.* (2014) [13]	LDV 6x6 rod bundle $Re = 6600 - 70{,}300$	Standard grid	Investigation of the turbulent flow
Qu *et al.* (2019) [14]	PIV 5x5 rod bundle $Re = 39{,}600$	Mixing vane	Systematically optimization of PIV for lateral flow measurements / analysis of systematic and random errors

Table 1: Summary of experimental studies on flow in rod bundles taken from the literature.

Bhattacharjee *et al.* [15] showed, that a square spacer grid with two mixing vanes has as much influence on the flow hydrodynamics as a circular spacer grid equipped with two symmetric mixing vanes. Chang *et al.* [1] found, that a split vane generates higher turbulence intensity and anisotropy than a swirl type vane. Kim *et al.* [16] showed, that split vanes, which produce flow separation because of the adverse pressure gradient near the rod surfaces, prevent cross-flow. Cui *et al.* [17] showed, that the swirl factor peaks at position $L \approx 4\ D_h$ for various vane types, namely for vanes with a 35° twist angle, vanes with a 45° twist, and split vanes. Wu *et al.* [18] found, that a 45° vane angle generates more persistent flow vortices in planes normal to the streamwise direction. Chang *et al.* [2] found, that a split vane provides a better mixing efficiency between the sub-channels than a swirl vane. They concluded, that a 25° vane angle is best and, that a 35° vane angle is unfavourable. Cheng *et al.* [19] showed, that the mixing coefficient, defined as the ratio of lateral velocity to mean entrance velocity, increases with both the vane angle and the length of the split vane. Wang *et al.* [3] found, that the mixing rapidly decreases from the vane tip $L = 0$ to $L \approx 4\ D_h$. In the work of In [20], split-vanes and twisted-vanes were found to provide a higher mixing rate for both swirl and cross-flow than side-supported vanes and swirl vanes. Shen *et al.* [4] showed, that a higher vane angle generally results in a higher mixing and a more heterogeneous mixing rate.

In the presence of spacer grid, the flow velocity is strongly anisotropic due to high swirling flow dynamics, flow separation, and sudden changes in the strain rate. Hence, the choice of a suitable turbulence model is crucial to achieving an accurate flow prediction. Numerous studies focusing on the turbulence modelling of the flow in rod bundles can be found in the literature (See Table 2 for a recent summary).

Researchers	Turbulence model	Simulation condition	Spacer grid type	Aim of the study
Kim *et al.* (2005) [16]	Standard k-ε	Two sub-channel Wall function	Split vane (25°) Split vane with cut-out (29°)	Optimization of shape of the mixing vanes/understanding flow characteristics and heat transfer
Bhattacharjee *et al.* (2017) [15]	Large eddy simulations (LES)	flow around a rod $Re = 8900$ y+ = 3	Square spacer grid Circular spacer grid Mixing vane (30°)	Effect of mixing vane on flow hydrodynamics
Cui *et al.* (2003) [17]	Standard k-ε	Single sub-channel $Re = 80{,}000$	NJ type vane (25°) Split vane (25°)	Effect of different vane shapes on flow structure and heat transfer
Wu *et al.* (2017) [18]	Standard k-ε, SST k-ω, RSM	Four sub-channel $Re = 40{,}000 - 120{,}000$ Wall function	Rectangular longitudinal vortex generators (30°,45°, 60°)	Thermal-hydraulic characteristics of the sub-channel/effect of vane angle
Cheng *et al.* (2017) [19]	SST k-ω	5x5 rod bundle	Split vane (25°, 31°, 37°,43°)	Influence of vane angle and vane length
In (2001) [20]	Standard k-ε	Single sub-channel $Re = 65{,}000$ y+ = 15	Split vane (30°) Side-supported vane Swirl vane Twisted vane (35°)	Impact of the vane angle on the induced swirl flow structure and the turbulent kinetic energy
Díaz *et al.* (2015) [21]	Standard k-ε, RNG k-ε Realizable k-ε, Standard k-ω, SST k-ω	flow around a pipe $Re = 40{,}000$ Wall function	Swirl disturbance generators	Comparison of the different Reynolds-Averaged Navier-Stokes (RANS) models
Gandhir *et al.* (2011) [22]	Realizable k-ε, SST k-ω	5 x 5 rod bundle $Re = 23{,}000$	Split vane	Examination of the effect of the selection of an appropriate turbulence model
Hosokawa *et al.* (2012) [23]	Standard k-ε, Launder–Sharma k–ε model	2x2 rod bundle $Re = 25{,}000$ y+ = 4-30	Standard grid	Measurements of 3D velocity and turbulence intensities/ comparison with the simulations
Xiong *et al.* (2014) [24]	SSG RSM, baseline RSM	3x3 rod bundle $Re = 15{,}200$ Wall function	Standard grid	Validation against experimental results
Holloway *et al.* (2006) [25]	Realizable k-ε, SST k-ω, RSM	Two sub-channel $Re = 35{,}000$ y+ ~ 1	Split vane (30°)	Investigation of the swirl flow and vortex effects downstream of the vanes
Conner *et al.* (2010) [26]	RNG k-ε	5 x 5 rod bundle y+ = 40-100	Split vane	Effect of computational mesh, turbulence model and the boundary conditions with comparison to benchmark experiments
Cinosi *et al.* (2014) [27]	Standard k-ε , Standard k-ω, RSM	5 x 5 rod bundle $Re = 50{,}000$ y+ = 0.05-7	Split vane (30°)	Improvement of the modelling with validation of MATiS-H (Measurements & Analysis of Turbulence in Subchannels – Horizontal) tests
Podila *et al.* (2016) [28]	Realizable k-ε, SST k-ω, RSM	5 x 5 rod bundle $Re = 50{,}000$ y+ = 0.04-40	Split vane	Prediction of the turbulence intensities and velocity variation downstream of the split-vane spacer grid
Chen *et al.* (2017) [29]	Standard k-ε, Realizable k-ε, RNG k-ε, RSM, SST k-ω	Four sub-channel y+ = 30-60	Split vane	Hybrid application of multiple Reynolds Averaged Navier-Stokes (RANS) models for the computational efficiency
Chen *et al.* (2017) [30]	RNG k-ε, SST k-ω, Standard k-ε, BSL RSM	5x5 rod bundle $Re = 14{,}600 - 34{,}800$ y+ = 30	Split vane	Selection of an appropriate turbulence model
Chen *et al.* (2016) [31]	Standard k-ε, Realizable k-ε, RNG k-ε	5 x 5 rod bundle $Re = 20{,}000$ y+ = 31-42	Split vane Hybrid vane	Investigation on thermal-hydraulic behaviour downstream of the spacer grid
Xiong *et al.* (2018) [32]	Standard k-ε Realizable k-ε	4 x 4 rod bundle y+ = 1	Twisted vane (35°)	Accuracy of Standard and Realizable k-ε model in predicting the swirling flow/ decay of swirling flow/evolution of turbulence
Koncar *et al.* (2018) [33]	SST- Scale adaptive simulation (SAS)	5 x 5 rod bundle $Re = 50{,}000$ y+ = 0.2-10	Split vane	Comparison of MATiS-H test results with flow simulations
Li *et al.* (2014) [34]	SST k-ω	5x5 rod bundle Wall function	Split vane (25°)	Computational effort of numerical methods for 17x17 large bundles
Chen *et al.* (2016) [35]	Standard k-ε, Realizable k-ε, RNG k-ε, SST k-ω, RSM	4x4 rod bundle 2x2 rod bundle	Split vane Swirl vane	Effect of simplified boundaries and region size
Liu *et al.* (2012) [36]	SST k-ω, Realizable k-ε, RNG k-ε, Standard k-ω , RSM	5x5 rod bundle Four sub-channel $Re = 28{,}000 - 42{,}000$ y+ < 1	Standard grid Split vane (30°)	Effect of boundary conditions, turbulence model, mesh refinement and turbulence near-wall treatment
Tseng *et al.* (2014) [37]	SST k-ω	Two sub-channel $Re = 35{,}000$	Split vane (30°)	Investigation of the thermal–hydraulic characteristics in a rod bundle with split-vane pair grids
Liu *et al.* (2010) [38]	RSM	Four sub-channel $Re = 28{,}000$ y+ = 31-48	Standard grid Split vane (30°)	Investigation of the effects of different types of grid on the turbulent mixing and heat transfer enhancement
Lifante *et al.* (2014) [39]	SST k-ω, BSL RSM	3x3 rod bundle y+ ~ 4	Standard grid	Analysis of secondary flow
Agbodemegbe *et al.* (2016) [40]	Non-linear standard k-ε, SST k-ω, Realizable k-ε	5x5 rod bundle $Re = 34{,}000$ y+ = 11-31	Split vane (30°)	Investigation of predictability of CFD/analysis of effect of split vane on cross-flow

Ikeda *et al.* (2006) [41]	Standard k-ε,	5x5 rod bundle y+ = 30-100	Split vane	Calculation of pressure loss in strap and mixing vane structures/ investigation of CFD applicability for predicting the CHF
Navarro *et al.* (2011) [42]	Standard k-ε	5 x 5 rod bundle Wall function	Split vane (25°)	Performance of CFD models by comparison with the experimental data taken from the literature
Sohag *et al.* (2017) [43]	Standard k-ε, Realizable k-ε, Standard k-ω, SST k-ω, RSM	1/8th of a sub-channel $Re = 1640 - 12{,}000$ y+ ~ 1	Standard grid	Investigation of spacer grid blockage ratio and grid spacing with different Re and P/D ratio
Mao *et al.* (2017) [44]	SST k-ω	5x5 rod bundle	Split vane	Investigation of mixing vane cross-flow in sub-channel
Lee *et al.* (2014) [45]	Standard k-ε, SST k-ω, RSM, SST- SAS, Direct /Large Eddy simulations	5 x 5 rod bundle $Re = 50{,}000$	Split vane	Validation of CFD codes based on the MATiS-H test by synthesizing different numerical studies.
In *et al.* (2008) [46]	Standard k-ε , RNG k-ε	Four sub-channel $Re = 28{,}000 - 42{,}000$ $Re = 500{,}000$ Wall function	Split vane (30°) Hybrid vane	Understanding the heat transfer enhancement/ comparison of the thermal-hydraulic performance for two different mixing vane spacers

Table 2: Summary of the numerical studies on rod bundle taken from the literature.

Díaz *et al.* [21] found, that in the swirl area downstream of the spacer grid, the Standard k-ε turbulence model is able to simulate the turbulent flow more accurately than the k-ω model. Gandhir *et al.* [22] found, that the Shear Stress Transport (SST) k-ω model provides more accurate results than its Realizable k-ε counterpart in terms of pressure drop. Hosokawa *et al.* [23] found, that the k-ε model yields good predictions for the axial velocity distribution in the sub-channel. Xiong *et al.* [24] found, that the Speziale-Sarkar-Gatski (SSG) model and the baseline Reynolds Stress Model (bRSM) result in higher axial velocities in the interior and edges of the sub-channel than in the experiments. Holloway *et al.* [25] showed, that the SST turbulence model delivers better results than the Realizable k-ε and RSM in terms of turbulence intensities. Conner *et al.* [26] showed that the Re-Normalization Group (RNG) k-ε model delivers results matching best the experimental data. Cinosi *et al.* [27] found, that the k-ε, k-ω, and the Reynolds Stress Turbulence (RST) models underestimate the time-averaged fluctuating velocity components u'. Podila *et al.* [28] simulated the flow in a rod bundle with the Realizable k-ε, the SST k-ω and the RSM models and found, that all turbulence models under-predict the measured turbulence intensity downstream of the split-vanes. In terms of flow anisotropy in the sub-channel, Chen *et al.* [29] obtained similar results with both the RSM and the RNG k-ε models. Chen *et al.* [30] found that, at high Reynolds number ($Re = 34{,}800$), the SST and the bRSM models deliver results better than the k-ε model in terms of axial velocity. They also found, that at lower Reynolds number ($Re = 14{,}600$), results are better with the k-ε and the RNG k-ε models. Chen *et al.* [31] also tested various turbulence models and found, that the RNG k-ε model predicts the rotational flow in the sub-channels most accurately. Simulations by Xiong *et al.* [32] indicated, that both the Realizable k-ε model with curvature correction and the Standard k-ε model with cubic-closure correction over-predict the decay of the swirling flow with the length (L). Koncar *et al.* [33] compared the Scale-Adaptive Simulation (SAS) model with an Unsteady Reynolds-averaged Navier-Stokes (URANS)-SST simulation and found, that it achieves a better agreement than the steady SST k-ω model in terms of velocity.

1.2 Heat transfer downstream of the spacer grid

Heat transfer enhancement by spacer grids and vanes was also analyzed by several researchers. Simulations by Liu *et al.* [36] showed good predictions of the Nusselt number at $Re = 28{,}000$. Tseng *et al.* [37] found an anisotropic heat transfer distribution on the rod surfaces in the azimuthal direction. Holloway *et al.* [5] reported, that in the presence of split-type vanes, the heat transfer coefficient first increases in the region $0 < L < 1.5D_h$ and then decreases exponentially with the streamwise distance L. Byun *et al.* [6] also showed, that for the split vane, the heat transfer enhancement occurs in the region $0 < L < 10D_h$. With the exception of the split vane design, Liu *et al.* [38] found, that CFD is able to predict reasonably well the downstream evolution of Nusselt number $Nu(L)$. In *et al.* [7] experimentally found, that the heat transfer coefficient downstream of the twist vane ($L > 0$) is up by about 30% compared to the region upstream of the vanes ($L < 0$). Moon *et al.* [8] showed, that heat transfer enhancement is only observable beyond $Re > 10{,}000$. Vane angle and vane type have also been found to significantly influence the heat transfer enhancement. Wu *et al.* [18] showed, that a 45° vane angle provides the largest heat transfer rate along the sub-channel. Findings of Kim *et al.* [16] showed, that the split vanes, cause the occurrence of temperature peaks at the rod surfaces.

1.3 Conclusion to the above current state of the art and motivations of this work

As can be seen in Table 1 and Table 2, either the swirl factor, or the mixing coefficient, or the pressure drop were taken into account to assess the optimum vane angle. Only very few authors actually combined those three parameters (swirl factor, mixing coefficient, pressure drop) in a single study. The above literature analysis shows that the following gaps have not yet been bridged:

- The majority of the studies were done with a vane angle close to 30 ± 2°. The shape evolution of the flow vortex was not yet studied in detail for other vane angles. More insight into the dynamics of the vortex formation and its decay downstream of the spacer grid is needed.
- Further studies on vane design explaining how cross and swirl flows affect the heat transfer are needed. A more detailed analysis of cross and swirl flow changes for different vane angles contributes to understanding the flow hydrodynamics.
- Only the studies in References [4, 18, 19] considered the effect of the vane and twist angles. Yet, heat transfer was not taken into account except in Reference [18].

Analysis of the above state-of-the-art literature also showed, that there still exists a general disagreement about the choice for the RANS turbulence model. In this paper, we therefore analyze numerically the effect of the vane angle on deformation rate, swirl flow, cross-flow, heat transfer, and pressure drop.

2. Methods

As illustrated in Figure 1, the present study focusses on a vortex generating split type vane arrangement since this vane type is the most common one [1-3, 11-12, 25-31]. One sub-channel was modelled to investigate the mixing rate. The two inclined vanes in the center of the sub-channel cause the flow downstream of the spacer to swirl [16].

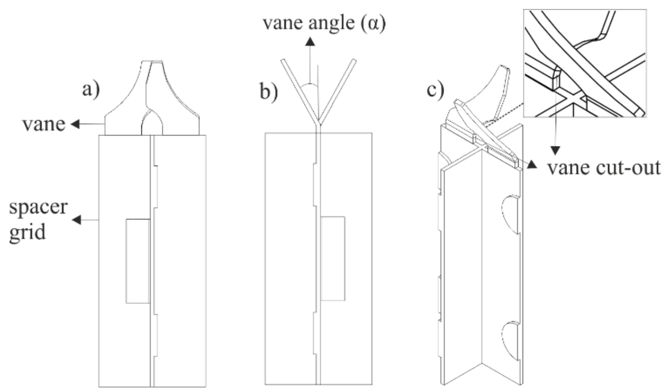

Figure 1: Schematic of the investigated grid spacer equipped with two split vanes: a) front view b) side view c) cross view.

The numerical domain consists of a bounded box containing a 3x3 rod arrangement. Each rod has an axial extension of 640 mm. A spacer grid is located 100 mm downstream of the inlet. The rod diameter is set to $D = 10$ mm with a bundle pitch set to $P = 12.8$ mm. The spacer grid has a length of $l_{\text{spacer}} = 30$ mm and thickness of 0.5 mm. The flow was simulated for the following six configurations of the spacer grid:

- a rod bundle framed in a spacer grid equipped with no vanes as a reference case,

- a rod bundle framed in a spacer grid equipped with split vanes, whose angles were set to $\alpha = 20°, 25°, 29°, 32°$, and $40°$.

Steady flow simulations were performed using the flow solver ANSYS CFX 18.2. Figure 2 shows a schematic of the rod bundle geometry presently used. The boundary conditions were set as follows:

- uniform heat flux of 20,000 W/m^2 at rod surfaces,

- constant atmospheric pressure at outlet,

- inlet with a temperature of 290 K,

- inlet with a velocity of U = 0.25 m/s,

- inlet turbulence intensity set to 5 %.

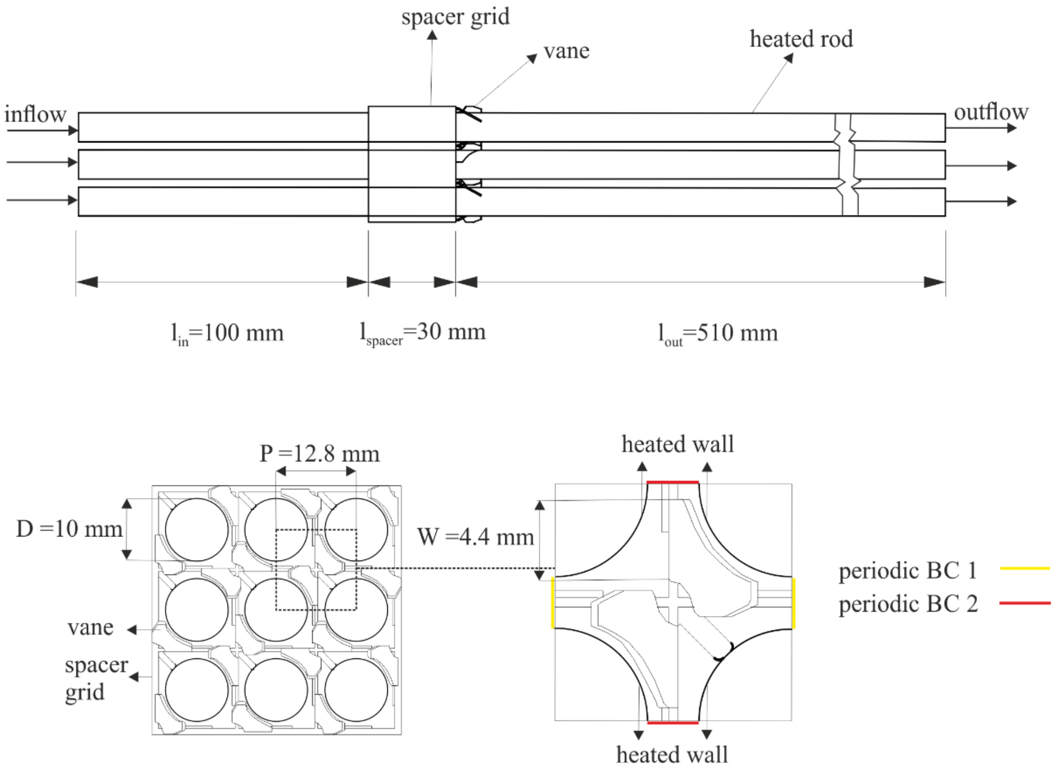

Figure 2: Schematic view of 3x3 rod bundle geometry with spacer grid and split type vanes.

The Reynolds number was set to Re = 14,000 in all subsequent calculations. Note, that the Reynolds number and the surface heat flux are set to relatively low values compared to the nominal ones under normal operating conditions. These chosen values enabled us comparative simulations with both a suitable mesh resolution near the wall ($y^+ < 1$) and an accurate heat transfer prediction at an affordable computational cost. Instead of using wall functions, the flow in near wall region was resolved. A no-slip boundary condition was assigned to all walls and periodicity was enforced to the sidewalls of the domain. Three different turbulence models were studied (Section 3.1) and eventually the RNG k-ε model was selected. The fluid was incompressible. The convergence criterion was set by making sure the RMS residuals fell below 10^{-6} for the continuity, momentum, energy and all turbulent quantities.

2.1 Governing equations

The flow dynamics and the heat transfer are described by the continuity equation

$$\frac{\partial \rho}{\partial t} + \frac{\partial}{\partial x_i}(\rho u_i) = 0, \tag{7}$$

the momentum equation

$$\frac{\partial}{\partial t}(\rho u_i) + \frac{\partial}{\partial x_i}(\rho u_i u_j) = -\frac{\partial p}{\partial x_i} + \frac{\partial \tau_{ij}}{\partial x_j} + \rho g_i, \tag{8}$$

$$\tau_{ij} = \mu^* \frac{\partial u_i}{\partial x_j}\,, \mu^* = \mu + \mu_t, \tag{9}$$

and the energy equation

$$\frac{\partial}{\partial t}(\rho c_p T) + \frac{\partial}{\partial x_i}(\rho c_p u_i T) = \frac{\partial}{\partial x_i}\left(\lambda \frac{\partial T}{\partial x_i}\right). \tag{10}$$

Where ρ is the fluid density, $u_{i=0,1,2}$ is the velocity component in the i-th direction, p is the pressure, τ_{ij} is the stress tensor, c_p is the specific heat coefficient, λ is the thermal conductivity, μ^* is the total viscosity, μ is the dynamic viscosity, μ_t is the turbulent viscosity, t is the time and T is the temperature. These differential equations are solved numerically along the x, y and z directions. In the present study, the Shear Stress Transport (SST), the k-ε Explicit Algebraic Reynolds Stress Model (EARSM) and the Re-Normalisation group (RNG) turbulence models were considered.

2.1.1 Shear Stress Transport (SST) model

The SST model [48] takes advantage of the k-ε and k-ω [49] turbulence models. For the free-stream flow far from the wall, the model uses the k-ε equations and switches to the k-ω equations in the near wall region. The choice for this turbulence model is based on the fact, that the SST turbulence model supposedly delivers a good prediction of separating flow with large normal strain and strong acceleration around the split vane regions [37]. With a fine mesh resolution, as is the case here, the k-ε and k-ω turbulence models are known to exhibit a good performance in estimating the pressure drop and velocity profiles, yet they do not perform very well in simulating rotational flows because of the absence of a rotational flow source term in the governing equation [22, 27].

2.1.2 Explicit Algebraic Reynolds Stress Model (EARSM) model

The Explicit Algebraic Reynolds Stress Model [50] is derived from the Reynolds stress transport equations, which enables the extension of the k-ε and baseline turbulence models to better capture the secondary flow effects. The selection of this model is motivated by the fact that the Reynolds stresses are solved using the anisotropy tensor given by pressure-strain correlation. The anisotropy tensor is the solution of an algebraic matrix equation, which depends on the strain and rotation tensors.

2.1.3 RNG k-epsilon

The RNG k-ε model was also selected for this study because it contains an additional term for the turbulence production and is supposedly better for swirling flows [51].

2.2 Mesh independence studies

Many authors previously used the pressure as convergence indicator in their mesh independence study [30, 34, 42]. Because the present work involves turbulence and heat transfer, two additional parameters, namely the turbulent kinetic energy k and the Nusselt number Nu, were also used as indicator. Calculations for the mesh study were done with the RNG k-ε model. Figure 3 shows the mean component of the total static pressure along the axial direction for increasing mesh densities. The simulations were performed with a vane angle set to 29°. It can be seen that the pressure evolution is hardly sensitive to the mesh density. We also note that the grid spacer causes a pressure drop of approximately 100 Pa.

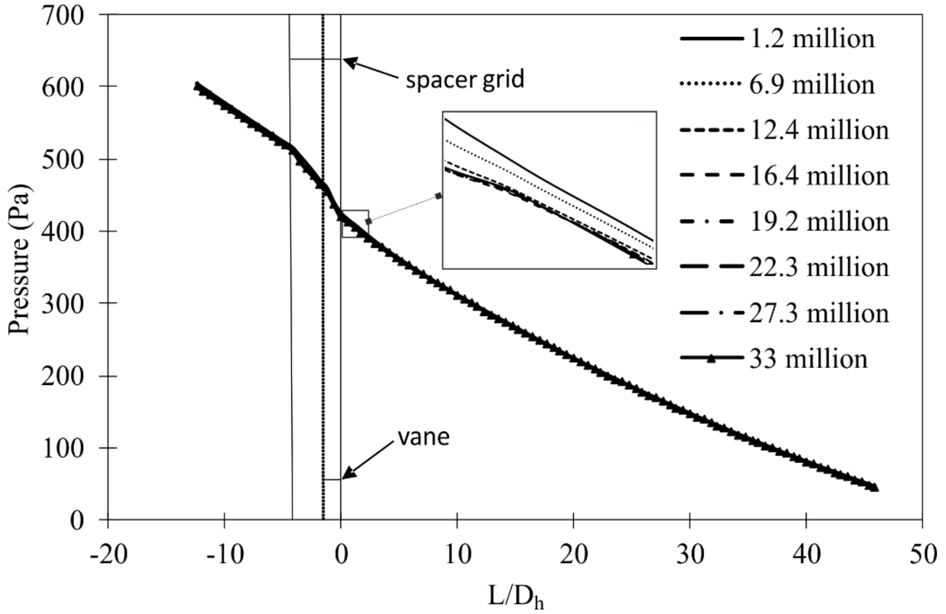

Figure 3: Effect of grid refinement on the mean component of the total static pressure P(L).

A hybrid mesh was used to discretize the flow domain. A tetrahedral mesh near the spacer and the vanes was used to account for the large flow anisotropy. In the remaining volume, a hexahedral mesh was used. Figure 4 shows exemplarily three different meshes with 6.9 million elements (mesh 1, subfigure a), 12.4 million elements (mesh 2, subfigure b), and 33 million elements (mesh 2, subfigure c). Their minimum and the maximum mesh size elements are 0.012 mm and 0.26 mm for mesh 1, 0.016 mm and 0.22 mm for mesh 2, and 0.017 mm and 0.15 mm for mesh 3.

Figure 4: Hybrid meshes with a) 6.9 million, b) 12.4 million, and c) 33 million elements.

Figure 5 shows the simulated mean turbulent kinetic energy (TKE) along the axial direction for increasing mesh densities. Upstream of to the spacer grid, the mean TKE is very much mesh independent. The effect of mesh refinement is largely noticeable within and downstream of the grid spacer in the region $0 < L < 12D_h$. We also found that a grid with 12.4 million is sufficient.

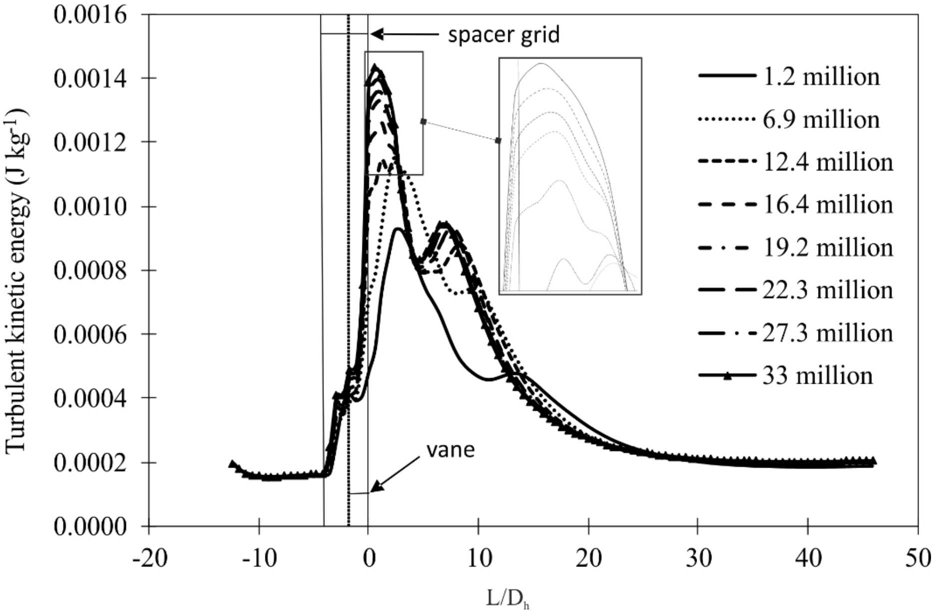

Figure 5: Effect of grid refinement on the mean turbulent kinetic energy k(x).

Figure 6 shows the simulated Nusselt number along the axial direction for increasing mesh densities. Similarly, the effect of mesh refinement is largely noticeable within and downstream of the spacer grid, in the region $0 < L < 5D_h$. It is found, that a minimum number of about N=12.10^6 of grid points is necessary to reach mesh-independency in the axial evolution Nu.

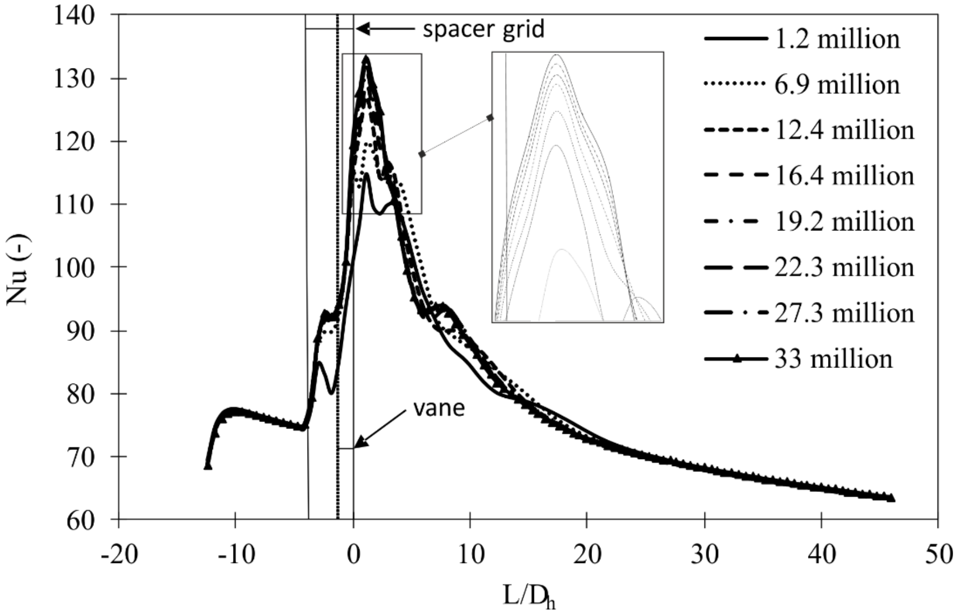

Figure 6: Effect of grid refinement on the Nusselt number Nu(x).

Table 3 summarizes the relative change in the integral value of the pressure, the TKE, and Nu. To reduce the computational effort, all subsequent simulations presented in this work were performed with a grid number set to N=12.4x10^6, resulting in relative average change below 1% for the pressure, below 3% for the TKE, and below 1% for the Nusselt number.

	Average relative change		
Cell number [x10^6]	TKE [J kg^{-1}]	Nu [-]	Pressure [Pa]
1.2 – 6.9	10.96 %	1.79 %	< 1%
6.9 – 12.4	4.48 %	0.84 %	< 1%
12.4 – 16.4	2.61 %	0.58 %	< 1%
16.4 – 19.2	1.23 %	0.21 %	< 1%
19.2 – 22.3	1.08 %	0.19 %	< 1%
22.3 – 27.3	0.89 %	0.13 %	< 1%
27.3 – 33	0.57 %	0.10 %	< 1%

Table 3: Effect of grid refinement on the relative change in the integral value of the TKE, Nu, and P.

3. Results

3.1 Turbulence model

Figure 7 shows the evolution of the TKE, integrated in-plane, as a function of the distance from the vane. The TKE evolution was computed for the three selected turbulence models. Upstream of the spacer grid in the region $-12\ D_h < L < -3.7\ D_h$, the turbulence model has a negligible effect on the TKE. Within and downstream of the spacer grid, that is $L > -3.7\ D_h$, the SST and the EARSM models perform similarly. The results obtained with the RNG k-ε model however show a higher turbulence evolution throughout the entire downstream region. A first global maxima at position $L \approx 1\ D_h$ and a second maxima further downstream of the spacer at position $L \approx 10\ D_h$ can be observed. The presence of a second maxima in the TKE was also reported in the simulations performed by In [20] and by In *et al.* [46] using a k-ε turbulence model. Beyond the position $L > 24\ D_h$, all turbulence models lead to a simulated TKE reaching a constant plateau.

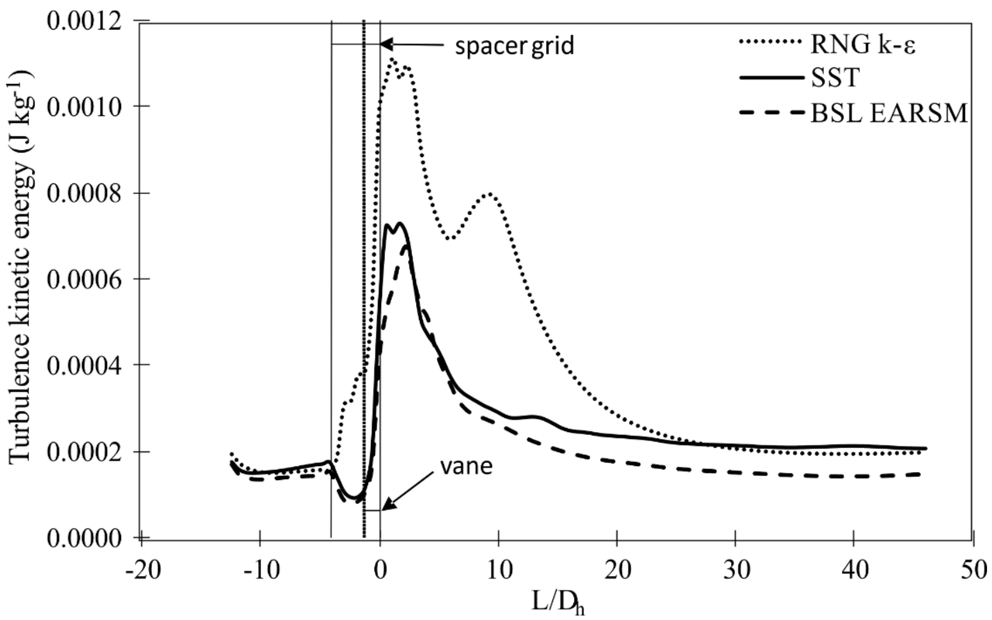

Figure 7: Turbulent kinetic energy distribution along the axial direction for a vane angle of 29°.

Published data from two experimental studies performed with split vanes and heated rods are available. The first one was performed by Holloway *et al.* [52] with water as coolant fluid. Because the rod had to be moved in the axial direction during in these experiments, the liquid flow and the thermal boundary layer were somewhat disturbed. Therefore, we decided to use the second experiment by Holloway *et al.* [5], in which the rod was fixed and air was the coolant fluid. In order to assess the performance of each turbulence model, we compared the simulation results with the experimental results provided by

Holloway *et al.* [5]. In their experimental tests, Holloway *et al.* [5] estimated an experimental uncertainty of Nusselt number about ±8.4%. For comparison purposes, the calculations were here repeated at Re = 29,000. Figure 8 shows the streamwise evolution of the average Nusselt number starting from $L = 0$. The in-plane averaged Nusselt number Nu (L) was normalized with the fully developed Nusselt number taken at position $L = 22D_h$ and calculated as $L_e/D_h = 4.4Re^{1/6}$.

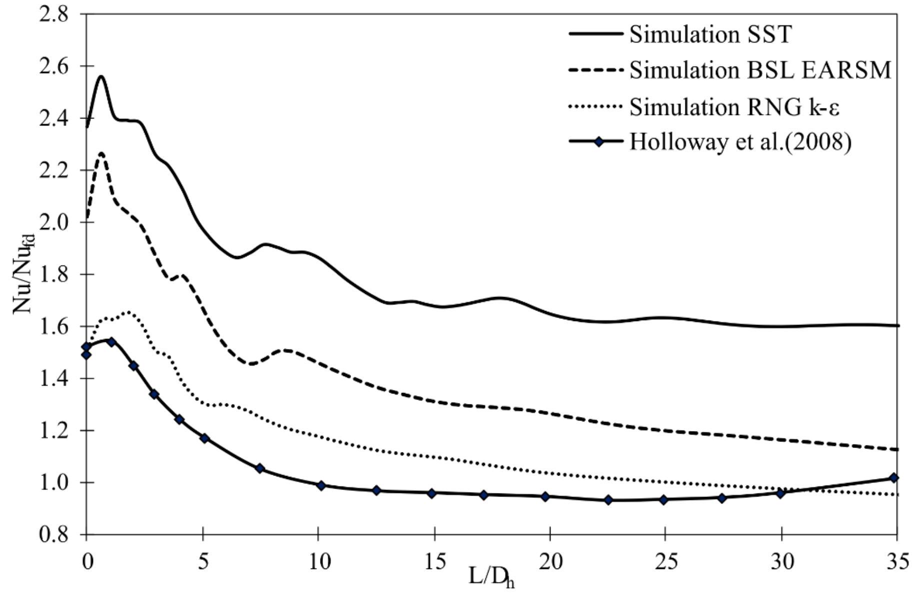

Figure 8: Evolution of the normalized Nusselt number for Re = 29,000 and a vane angle of 29°.

The axial evolution of the normalized Nusselt number shows that all selected turbulence models overestimated the experimentally determined Nusselt number. This overestimation is also backed up by the RANS simulations performed by Tseng *et al.* [37]. The SST and the EARSM turbulence models had here maximum errors estimated at about 84% and 45%, respectively. The findings also show that the RNG k-ε turbulence model performed best. It had a maximum error estimated at about 18%.

3.2 Deformation rate of the flow

To better understand the change in the fluid deformation induced by the vanes, the tensor of the velocity gradient [53],

$$\nabla \otimes \boldsymbol{U}|_{ij} = \boldsymbol{S}_{ij} + \boldsymbol{\Omega}_{ij} \tag{11}$$

with

$$\boldsymbol{S}_{ij} = \frac{1}{2}\left(\frac{\partial U_i}{\partial x_j} + \frac{\partial U_j}{\partial x_i}\right) \tag{12}$$

$$\boldsymbol{\Omega}_{ij} = +\frac{1}{2}\left(\frac{\partial U_i}{\partial x_j} - \frac{\partial U_j}{\partial x_i}\right), \tag{13}$$

was calculated for each vane angle. The tensor in Equation 11 is decomposed into a symmetric and an asymmetric part, which respectively describe the rate-of-strain $\boldsymbol{S}_{ij}$ and the rate-of-rotation $\boldsymbol{\Omega}_{ij}$ [54]. $\boldsymbol{S}_{ij}$ is a measure of the local folding and stretching of the flow and $\boldsymbol{\Omega}_{ij}$ is a measure of the local flow rotation. The reason behind separating the tensor $\nabla \otimes \boldsymbol{U}$ into a strain and a rotation part is to analyse the role played by the viscous stresses τ_{ij} (See Eq. 8). In fact, the strain component $\boldsymbol{S}_{ij}$ describes the flow motion that resists the viscous stresses, while the rotation component $\boldsymbol{\Omega_{ij}}$ describes the flow motion that is not counteracted by viscous stresses [53]. In the following, the effect of vorticity and strain is analyzed for each vane angle.

3.2.1 Vorticity

The vorticity vector $\boldsymbol{\omega} = \left[\omega_x \; \omega_y \; \omega_z\right]^T = \left[\Omega_{xx} \; \Omega_{yy} \; \Omega_{zz}\right]^T$ is defined using the diagonal components of rate-of-rotation tensor in Eq. 13. Results from the present simulations show that the magnitude of the axial component $|\omega_x|$ is up to eight times greater than the other two component magnitudes $|\omega_y|$ and $|\omega_z|$. Figure 9 illustrates the evolution of the mean x-component of the vorticity in the axial direction of the rod.

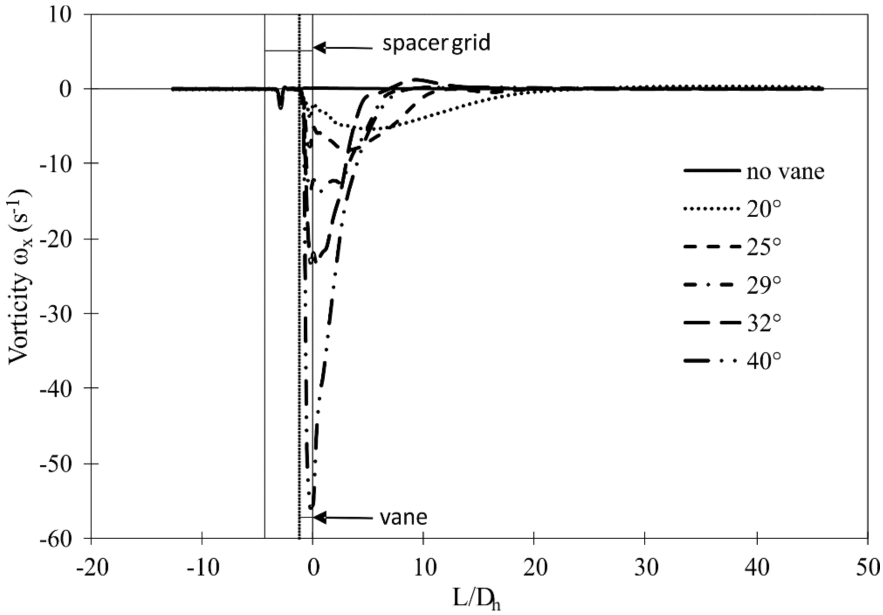

Figure 9: Axial component of vorticity distribution along the axial direction for different vane angles and no vane.

The spacer grid without the vanes causes a low vorticity throughout the entire sub-channel. In the presence of vanes, the vorticity reaches a maximum downstream of the spacer grid and eventually decreases to zero. With a 20° vane angle, the maximum vorticity is about $\omega_x = -5\ s^{-1}$ at a position around $L = 5.5\ D_h$ and it becomes zero further downstream at around $L = 19\ D_h$. With a 40° vane angle, the maximum vorticity is about $\omega_x = -55\ s^{-1}$ at a position around $L = 0$ and reached a zero value further downstream at around $L = 10\ D_h$. The present results also show that the maximum vorticity increases with the vane angle. When the vane angle rises from 20° to 40°, the maximum vorticity increases by up to a factor 10. The axial length, over which the flow is rotational, however, decreases with the vane angle. There exists an optimum vane angle, for which a trade-off between vorticity magnitude and axial length, is achieved.

3.2.2 Strain

The vanes produce a certain amount of shear strain rate resulting in deformation of the vortex downstream of the spacer grid. Strain and vorticity are the two main mechanisms responsible for the transfer of energy from the mean flow to the turbulence field. The production of turbulent energy is function of the strain rate S_{ij} and the turbulent velocity fluctuations. The production tensor is defined as [505]

$$P_{ij} = -\rho\, \overline{u_i u_j} S_{ij}. \tag{14}$$

The axial evolution of the average strain rate $\boldsymbol{S}_{xx}$, characterizing the deformation rate of the vortex by flow shearing in the *yz*-plane normal to the axial flow direction, is analysed. This tensor component is here of practical interest. Figure 10 compares the axial component of strain $\boldsymbol{S}_{xx}$ with the turbulent kinetic energy k along the axial direction downstream of the spacer grid. It can be seen that the peak in the turbulent kinetic energy roughly coincides with the peak also observed for the strain $\boldsymbol{S}_{xx}$.The strain effect disappears for all vane angles beyond about $L > 15\ D_h$.The results shown in Figure 10 are in line with Eq. (12). A higher strain results in a higher turbulent kinetic energy. 29° and 32° vane angles result in an improved shear deformation rate since the magnitude and effective length of strain have a better combination than other vane angles.

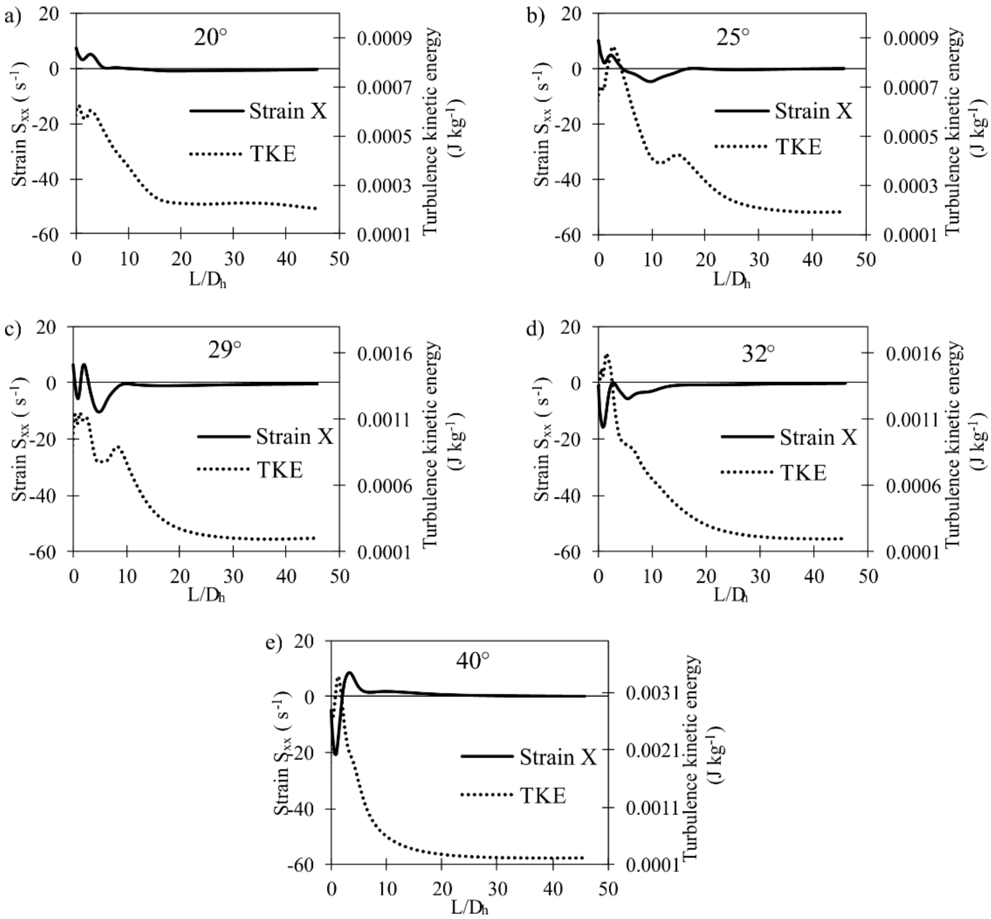

Figure 10: Axial component of the strain component S_{xx} and turbulent kinetic energy distribution along the axial direction for vane angles a) 20° b) 25° c) 29° d) 32° e) 40°.

3.2.3 Turbulent kinetic energy

Figure 11 shows the axial evolution of the turbulent kinetic energy, averaged in the yz-plane for each vane angle. Upstream of the vane, the TKE is hardly affected by the vane angle. The difference in the TKE evolution becomes noticeable when the coolant starts passing through the vanes. The effect of the vane angle of TKE closely resembles of the vorticity. The magnitude of the maxima increases with the vane angle while the axial length, over which the flow is highly turbulent, decreases with the vane angle. There exists an optimum vane angle with respect to straight of between high turbulent intensity and adequate axial length.

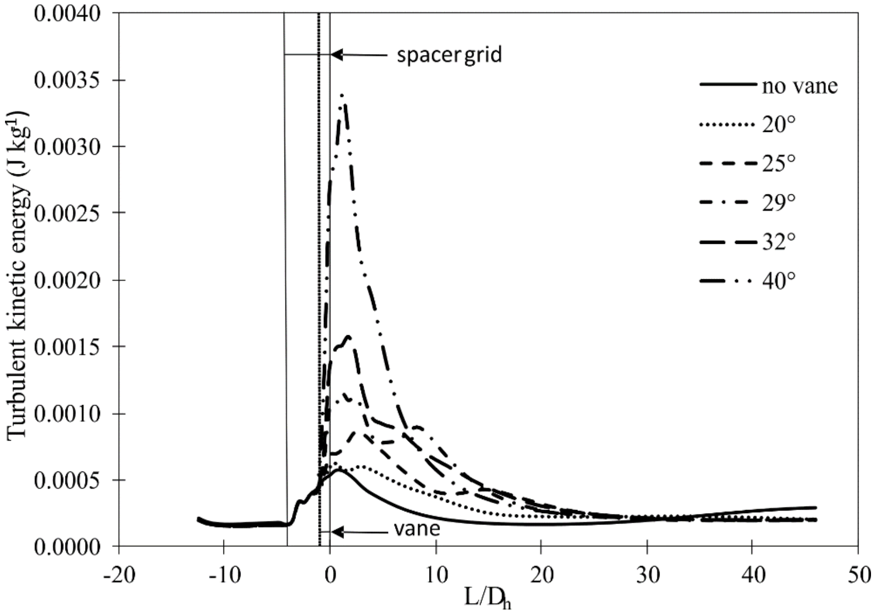

Figure 11: Axial evolution of the turbulent kinetic energy averaged in the yz-plane.

3.3 Secondary flow

The secondary flow, induced by the vanes and gradually decreasing downstream of the spacer grid, is here investigated. To assess the secondary flow quantitatively, the swirl factor was calculated as a function of the streamwise length L (See Eq. 5). Figure 12 shows the swirl factor along the downstream axis of the spacer grid. Very little flow swirl is observed for the no vane case. For vane angles above 20°, the swirl factor decreases exponentially with the length L. The swirl factor is lowest for 20° vane angle. Up to position $L = 2.3D_h$, the swirl factor is highest for 40° vane angle. In the intermediate range $2.3D_h < L < 4.5D_h$, the swirl factor is highest for 29° vane angle, closely followed by 32° vane angle. Beyond $L > 8D_h$, the swirl factor is highest for 32° vane angle downstream the vane. The vane angle 32° has the lowest swirl factor throughout.

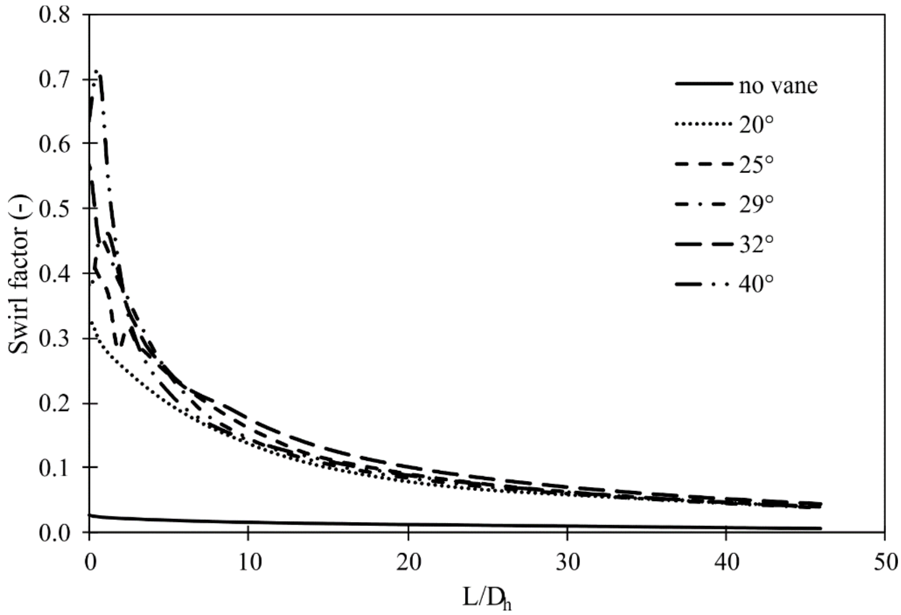

Figure 12: Axial variation of the swirl factor with increasing vane angle.

Figure 13 shows the cross-sectional pressure field at position $L = 0$ for each vane angle. As the fluid passes through the vanes, it causes a pressure modification in the yz-plane. This modified pressure field in-turn results in a flow vortex centered in the sub-channel.

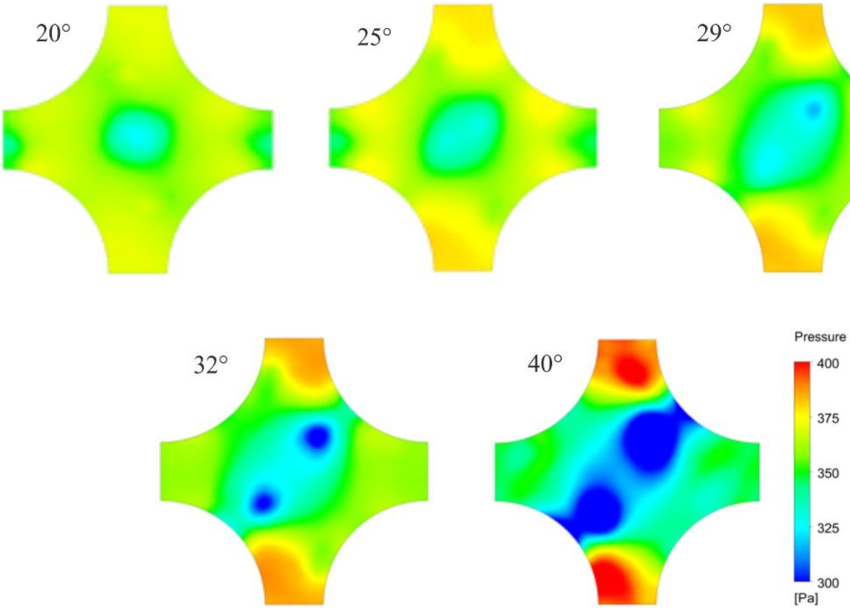

Figure 13: In-plane pressure distribution at $L = 0$ for vane angles.

As can be seen in Figure 14, right upstream of the vanes, the cross-sectional velocity field exhibits a characteristic S-shape with an inside velocity that is much lower than outside velocity. The maximum velocity approaches 0.35 m/s for the 29° vane angle. As the vane angle increases, the vortex region elongates. The maximum fluid velocity rises to 0.5 m/s for a 40° vane angle. Caution should however be given to the configuration involving the 40° vane angle. A low-pressure region exists in the boundary layer starting from this cut-out part of the vane. Consequently, flow separation occurs due to adverse pressure gradients. The blue low velocity regions in the core region of the sub-channel in Figure 14 illustrates the flow separation occurring for the 40° vane angle.

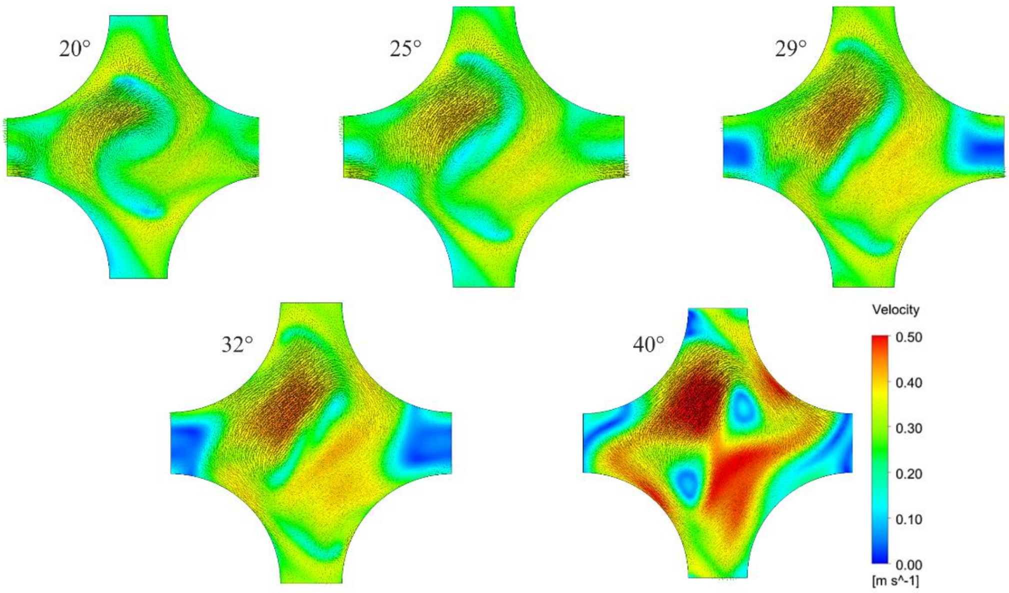

Figure 14: In-plane velocity distribution at $L = 0$ for vane angles.

Figure 15 represents the secondary flow velocity fields in three successive cross-sectional planes located at positions $L = 0, 1.8D_h$, and $5.5D_h$. It shows the flow field development for each vane angle.

For the 20° vane angle, an elongated circular vortex exists just downstream of the spacer grid at position $L = 0$. The left/right vane pattern creates a clockwise-rotating vortex region with negative vorticity at the centre of the sub-channel. Beside a dominant swirl flow superimposed with a slight cross-flow also exists. At position $L = 1.8D_h$ the swirl flow still persists. The magnitude of the cross-flow decreases and a small circulation region in the centre of the sub-channel can be seen. At position $L = 5.5D_h$, the centre of the vortex region migrates away from the sub-channel center. This movement positively affects the heat transfer from rod surfaces. On the other hand, other rod surfaces that are further away from the vortex region are negatively affected in terms of the heat transfer due to a decreasing mixing in this local region.

For the 25° vane angle, the vortex is more elongated at position $L = 0$ and a stronger vorticity is observed. At around $L = 1.8D_h$, a circular flow vortex and a circulation region appear in the sub-channel. At around $L = 5.5D_h$, the circular flow vortex moves to the left of the geometric center of the sub-channel. The migrated offset position of the vortex center is larger than that observed with the 20° vane angle.

For the 29° vane angle, a vortex of nearly rectangular shape forms at position $L = 0$. The strength of the vorticity is higher than for 25° vane angle. At this vary position, there are also smaller re-circulation regions of positive vorticity near the rods. At around $L = 1.8D_h$, the vortex becomes more oval in shape and migrates further leftwards from the geometric center of the sub-channel. This, in-turn, provides a better cross-flow. At around $L = 5.5D_h$, the vortex disappears and almost no more swirl flow can be observed. The cross-flow contributes here to an enhanced heat transfer than that obtained for the 20° and 25° vane angles. The lateral velocities also have higher magnitudes near the horizontal and vertical openings.

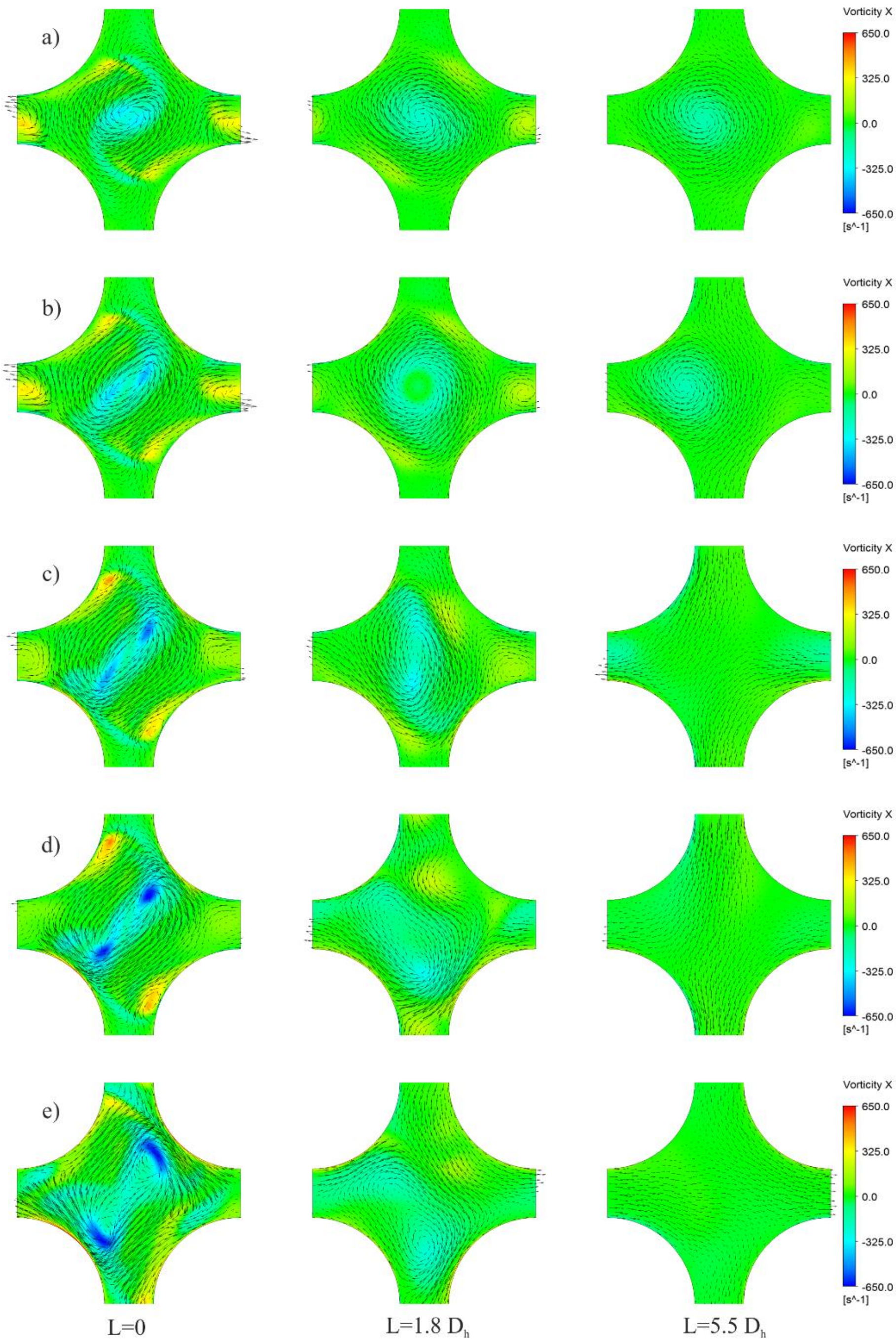

Figure 15: Axial vorticity fields and lateral velocity vectors for three different cross sections and vane angles a) 20° b) 25° c) 29° d) 32° e) 40°.

For the 32° vane angle, there exists a rectangular vortex at position $L = 0$. It covers a large area of the sub-channel cross-section. In this region, there are also two local high vorticity spots reaching high negative values. This dominant swirl flow prevents an effective cross-flow. Small flow re-circulations similar to 29° vane angle also are also present. At around $L = 1.8D_h$, the rectangular vortex becomes smaller and migrates to the side. This promotes a better cross-flow within the sub-channel. At around $L = 5.5D_h$, an uneven cross-flow distribution can be observed.

For the 40° vane angle, a dominant swirl flow occurs and it covers nearly the entire sub-channel at position $L = 0$. There are also two small vortices embedded in the large vortex region. In addition, the small re-circulation regions near the rod surfaces nearly disappear. At around $L = 1.8\ D_h$, these two small vortices move close to each other and migrate further bottom left of the sub-channel. At position $L = 5.5D_h$, the swirl flow disappears completely. This also causes an uneven cross-flow distribution.

Consequently, just after the vanes, strong swirl flow and weak cross-flow are present. As the vane angle increases, the vortex region directly downstream of the spacer grid changes in shape. At positions $L = 0$ and $L = 1.8D_h$, there is a strong swirl flow for all angles. The magnitude of the swirl flow decays with the axial length L. There is also a vortex in the sub-channel at position $L = 5.5D_h$ for the vane angle 20° and 25°. Yet, at this same position, this vortex region disappears for vane angles 29°, 32° and 40°. As the flow develops, the vortices tend to migrate leftwards from the geometric centre of the sub-channel. Holloway *et al.* [25] also observed a similar vortex migration in their experiments. This is contrary to their CFD results, which predicted a vortex in the geometric centre of the sub-channel. From the present results, we found that the 29° and 32° vane angles provide better cross and swirl flows, which are beneficial for an efficient heat transfer.

3.4 Heat transfer

Figure 16 illustrates the effect of the vane angle on the axial evolution of Nusselt number. It can be seen, that upstream of the spacer grid the vane angle has virtually no effect on the heat transfer. Right downstream of the spacer grid, the Nusselt number reaches maxima and eventually decreases exponentially with the length L. A higher vane angle results in a higher maximum. Compared to the no-vane configuration, a vane angle of 20°, 25°, 29°, 32° and 40° results in an increase of the average Nusselt number downstream of the spacer grid ($0 < L < 46\mathrm{D_h}$) of about 7.8%, 10.9%, 12.3%, 13.6%, and 15.5% respectively. With a 40° vane angle and in the region $0 < L < 8\mathrm{D_h}$, the Nusselt number is greater than anyone for a smaller vane angle. The Nusselt number evolution obtained with the 40° vane angle drops almost to the same level as for 29° vane angle at around $L = 10D_h$.The overall decay in the Nusselt number exhibits a trend similar to that reported earlier for the turbulent kinetic energy.

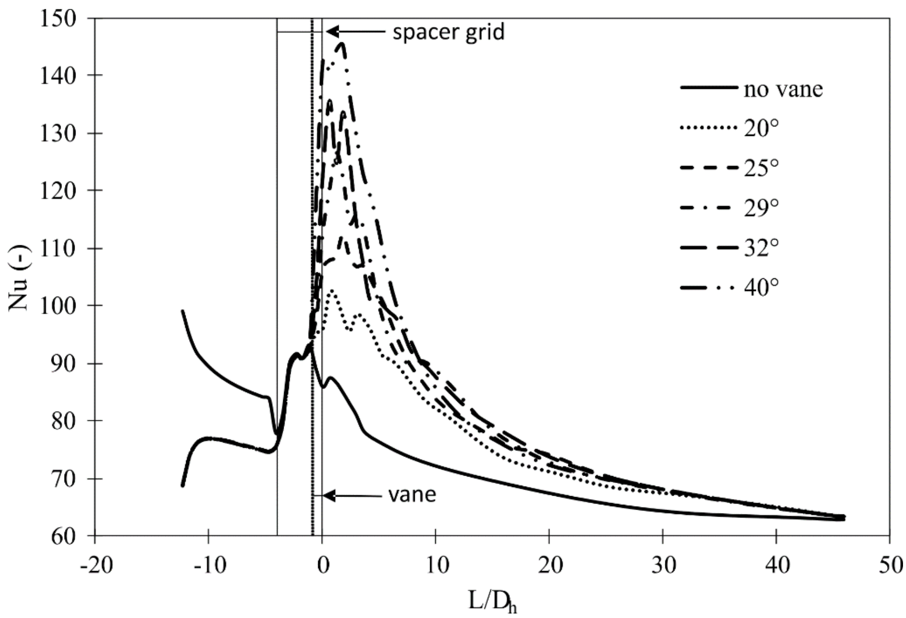

Figure 16: Effect of the vane angle on the axial evolution of Nusselt number.

An overlay of the flow vorticity with the Nusselt number is shown in Figure 17 for the vane angles $\alpha = 20°, 29°$ and $40°$. Only three angle were deliberately picked to not overload the figure with information. Results from this figure suggests, that heat transfer increases with the flow vorticity in the region $L < 8D_h$.

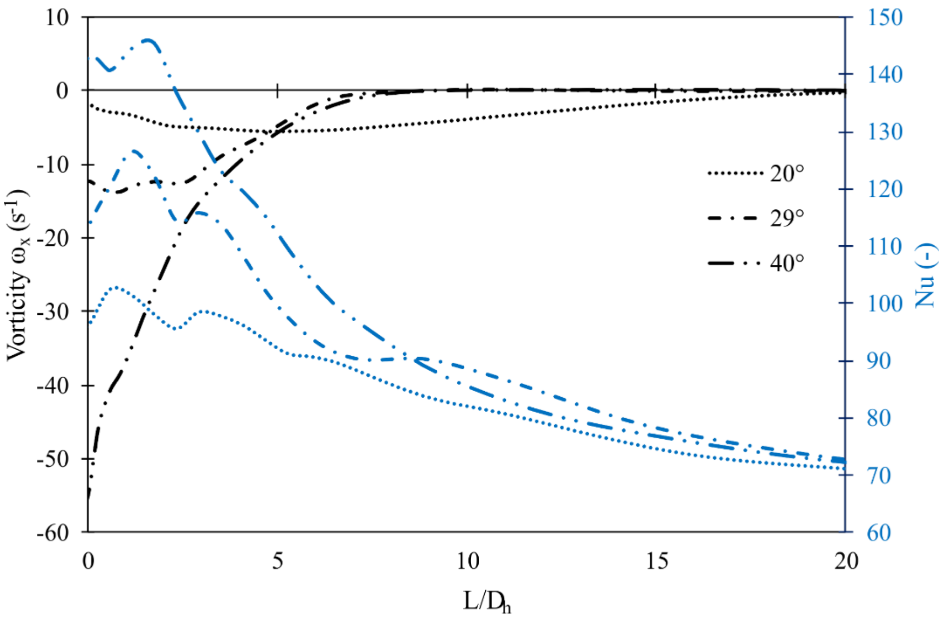

Figure 17: Axial evolution of Nusselt number versus vorticity for vane angles 20°, 29°and 40°.

Figure 18 shows the circumferential cross-sectional temperature distribution at three axial positions $L = 0$, $1.8\ D_h$, and $5.5\ D_h$. At $L = 0$, high temperature regions tend to disappear with increasing vane angle. With the exception of the 20° vane angle, the surface temperatures at position $L = 1.8D_h$ are comparatively low. Further downstream, at position $L = 5.5D_h$, high temperature regions occur for almost every vane angle. The results hence show that a higher vane angles results in a more homogeneous and efficient heat removal.

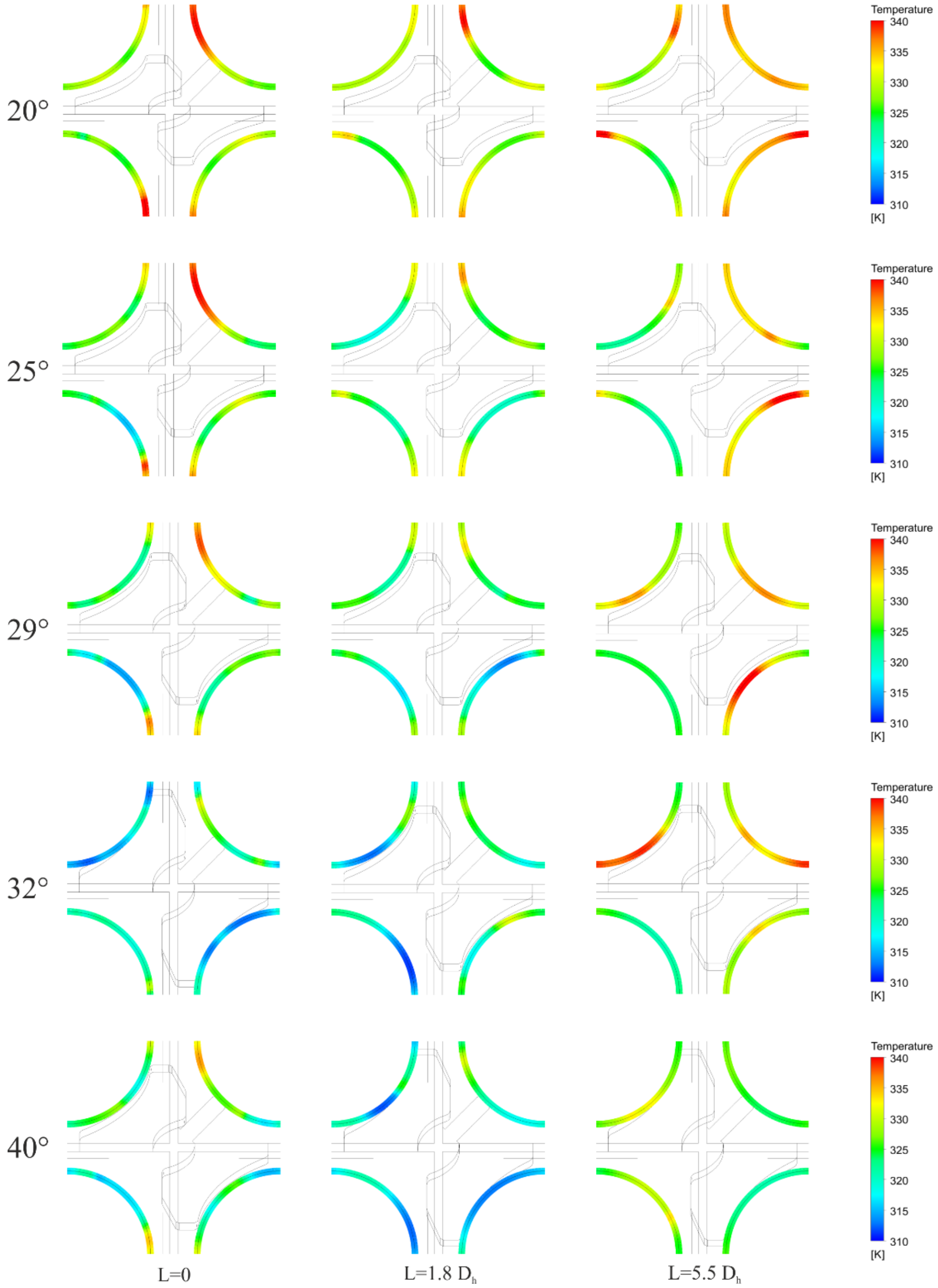

Figure 18: Circumferential cross-sectional temperature distribution at three axial positions.

3.5 Pressure drop

Pressure drop is another important engineering parameter for selecting the most appropriate vane angle. Figure 19 shows the total static pressure distribution in the axial direction for each vane angle.

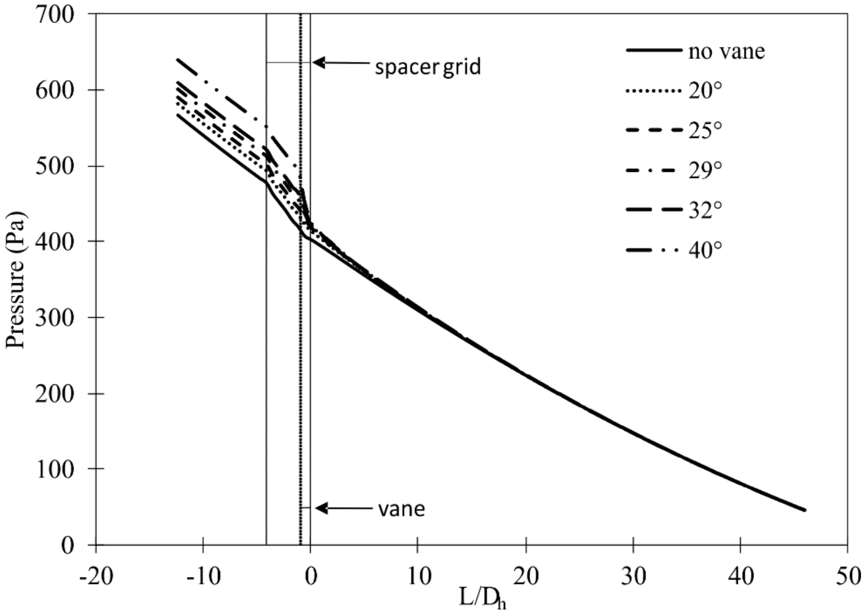

Figure 19: Effect of vane angle on pressure evolution

Upstream of the spacer grid the spacer without vanes leads to the lowest pressure and the spacer grid with a 40° vane angle leads to the highest pressure. For the intermediate vane angles, a higher vane angle generally results in a higher pressure. The spacer grid and the vanes are known to cause an increase in the pressure drop [20, 30]. The present results suggest a considerable pressure drop in the region $-4D_h < L < 0$. Further downstream, that is beyond $L > 5.5D_h$, the low axial decrease in the pressure is roughly identical for all vane angles. The spacer grid was found to contribute by far to the total pressure drop. Table 4 shows the increase in the pressure drop, calculated as $\Delta P = |P(L/D_h = 0) - P(L/D_h = -3.7)|$, as a function of the vane angle. The reference pressure drop is calculated using the no-vane simulation.

Angle	Pressure drop ΔP (Pa)	ΔP Increase (%) $|\Delta P_2 - \Delta P_1|/\Delta P_{\mathrm{ref}}$
No vane (Reference)	ΔP_{ref} = 68.33	Reference
20°	76.05	11.2 %
25°	80.39	17.6 %
29°	88.64	29.7 %
32°	95.86	40.2 %
40°	122.72	79.6 %

Table 4: Pressure difference between spacer grid inlet and just after the vanes.

Figure 20 shows the Nusselt number averaged over the area $-3.7 < L/D_h < 46$ as well as the pressure drop, calculated as $\Delta P = |P(L/D_h = -3.7) - P(L/D_h = 46)|$ against the vane angle. It can be seen that both the averaged Nusselt number and the pressure drop increase with the vane angle. Care should however be taken for larger vane angles. As previously discussed, a 40° vane angle results in flow separation. Thus, although a vane angle of 40° provides maximum average heat transfer there is a considerable pressure drop caused by the flow separation.

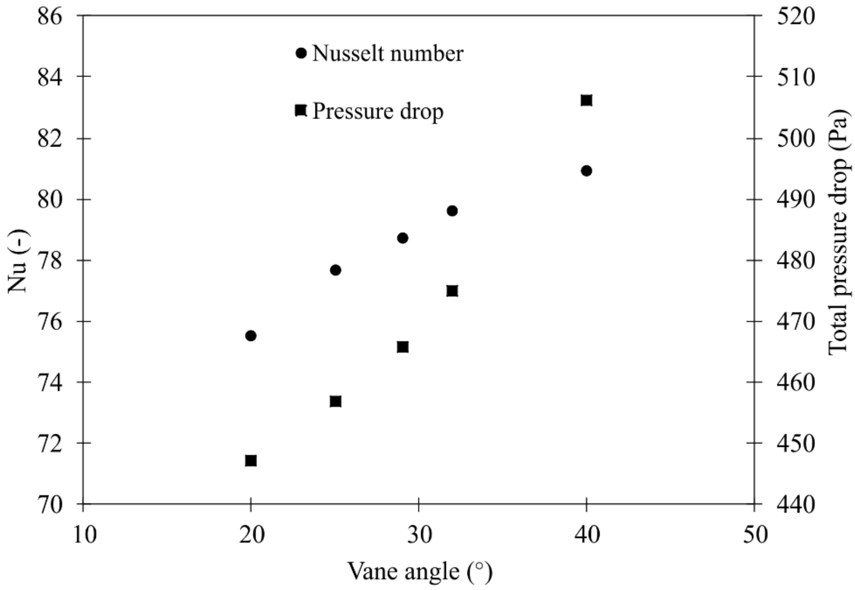

Figure 20: Nusselt number averaged over the area $-3.7 < L/D_h < 46$ as well as the pressure drop, calculated as $\Delta P = |P_{L/D_h=-3.7} - P_{L/D_h=46}|$, against vane angle.

4. Conclusions

A substantial state-of-the art review was provided in the beginning of this work and showed, that there is no agreed turbulence model for simulations of flow in sub-channel with spacer grid. Besides, most of the available studies did not consider flow development and heat transfer related to vane angle. Based on the available experimental and numerical studies, we performed numerical studies to elucidate the effect of the vane angle on various important key parameters, namely pressure drop, heat transfer, cross-flow and flow deformation. Findings from this numerical study can be summarized as follows:

1. The turbulent kinetic energy and the Nusselt number are decisive parameters and should be accounted for in the mesh convergence study.
2. Among the tested three turbulence models, the RNG k-ε model predicts the heat transfer most accurately.
3. Vorticity is not the only mechanism responsible for enhanced heat transfer downstream of the vane. Yet, it has a dominant effect in the region near the vane tip.
4. The shape and the center of the flow vortex downstream of the vane is a function of the vane angle. Irrespective of the vane angle, the vortex eventually migrates away from the sub-channel center. Some parts of the rod surfaces are hotter, which in-turn leads to an inhomogeneous heat transfer distribution in the sub-channel.
5. The swirl flow is very strong right downstream of the spacer grid. Swirl and cross flows result in highest heat transfer for 29 and 32° vane angles.
6. For 40° vane angle multiple flow vortices develop and create high pressure drop.
7. The 29 and 32° vane angles give a better heat transfer performance in terms of average cross sectional Nusselt number. Higher vane angle results in a more uniform temperature distribution on the rod surfaces.

The above results are quantitatively summarized in Table 5. Since the flow in the sub-channel is a developing flow, not only the local mixing and heat transfer efficiency but also the continuity and balance of these efficiencies along the whole sub-channel must be taken into account. In this context, it noticeable that a vane angle close to 30° provides a good trade-off between flow deformation, which affects the mixing efficiency, the secondary flow, the heat transfer, and the pressure loss. An optimal heat transfer due to efficient cross-flow from one sub-channel to another is also achieved.

Vane angle	20°	25°	29°	32°	40°
Measure of mixing efficiency	o	+	+++	+++	+
Secondary cross-flow efficiency	o	++	+++	+++	+
Swirl flow	o	++	++	+++	++
Heat transfer efficiency	o	+	++	++	+++
Pressure loss	o	+	++	++	+++
Note					flow separation

Table 5: Effect of vane angle on the different hydrodynamic and heat transfer parameters (o low effect, + moderate effect, ++ strong effect, +++ extreme effect).

5. References

1. Chang, S.K., et al., *Phenomenological investigations on the turbulent flow structures in a rod bundle array with mixing devices.* Nuclear Engineering and Design, 2008. **238**(3): p. 600-609.
2. Chang, S.K., S. Kim, and C.H. Song, *Turbulent mixing in a rod bundle with vaned spacer grids: OECD/NEA-KAERI CFD benchmark exercise test.* Nuclear Engineering and Design, 2014. **279**: p. 19-36.
3. Wang, X.Y., et al., *Flow visualization and mixing quantification in a rod bundle using laser induced fluorescence.* Nuclear Engineering and Design, 2016. **305**: p. 1-8.
4. Shen, Y.F., Z.D. Cao, and Q.G. Lu, *An Investigation of Cross-Flow Mixing Effect Caused by Grid Spacer with Mixing Blades in a Rod Bundle.* Nuclear Engineering and Design, 1991. **125**(2): p. 111-119.
5. Holloway, M.V., D.E. Beasley, and M.E. Conner, *Single-phase convective heat transfer in rod bundles.* Nuclear Engineering and Design, 2008. **238**(4): p. 848-858.
6. Byun, S.J., et al., *Experimental study on the heat transfer enhancement in sub-channels of 6 x 6 rod bundle with large scale vortex flow mixing vanes.* Nuclear Engineering and Design, 2018. **339**: p. 105-115.
7. In, W.K., C.H. Shin, and C.Y. Lee, *Convective heat transfer experiment of rod bundle flow with twist-vane spacer grid.* Nuclear Engineering and Design, 2015. **295**: p. 173-181.
8. Moon, S.K., et al., *Single-phase convective heat transfer enhancement by spacer grids in a rod bundle.* Journal of Nuclear Science and Technology, 2014. **51**(4): p. 543-557.
9. Han, S.Y., et al., *Measurements of the flow characteristics of the lateral flow in the 6 x 6 rod bundles with Tandem Arrangement Vanes.* Nuclear Engineering and Design, 2009. **239**(12): p. 2728-2736.
10. Caraghiaur, D., H. Anglart, and W. Frid, *Experimental investigation of turbulent flow through spacer grids in fuel rod bundles.* Nuclear Engineering and Design, 2009. **239**(10): p. 2013-2021.
11. Ikeda, K., *CFD application to advanced design for high efficiency spacer grid.* Nuclear Engineering and Design, 2014. **279**: p. 73-82.
12. McClusky, H.L., et al., *Mapping of the lateral flow field in typical subchannels of a support grid with vanes.* Journal of Fluids Engineering-Transactions of the Asme, 2003. **125**(6): p. 987-996.
13. Xiong, J.B., et al., *Experimental investigation on anisotropic turbulent flow in a 6 x 6 rod bundle with LDV.* Nuclear Engineering and Design, 2014. **278**: p. 333-343.
14. Qu, W.H., et al., *High-fidelity PIV measurement of cross flow in 5 x 5 rod bundle with mixing vane grids.* Nuclear Engineering and Design, 2019. **344**: p. 131-143.
15. Bhattacharjee, S., G. Ricciardi, and S. Viazzo, *Comparative study of the contribution of various PWR spacer grid components to hydrodynamic and wall pressure characteristics.* Nuclear Engineering and Design, 2017. **317**: p. 22-43.
16. Kim, K.Y. and J.W. Seo, *Numerical optimization for the design of a spacer grid with mixing vanes in a pressurized water reactor fuel assembly.* Nuclear Technology, 2005. **149**(1): p. 62-70.

17. Cui, X.Z. and K.Y. Kim, *Three-dimensional analysis of turbulent heat transfer and flow through mixing vane in a subchannel of nuclear reactor.* Journal of Nuclear Science and Technology, 2003. **40**(10): p. 719-724.
18. Wu, J.M., et al., *CFD analysis of the impact of a novel spacer grid with longitudinal vortex generators on the sub-channel flow and heat transfer of a rod bundle.* Nuclear Engineering and Design, 2017. **324**: p. 78-92.
19. Cheng, S.H., H.D. Chen, and X.Y. Zhang, *CFD analysis of flow field in a 5 x 5 rod bundle with multi-grid.* Annals of Nuclear Energy, 2017. **99**: p. 464-470.
20. In, W.K., *Numerical study of coolant mixing caused by the flow deflectors in a nuclear fuel bundle.* Nuclear Technology, 2001. **134**(2): p. 187-195.
21. Díaz, D.d.O. and D.F. Hinz, *Performance of eddy-viscosity turbulence models for predicting swirling pipe-flow: Simulations and laser-Doppler velocimetry.* arXiv preprint arXiv:1507.04648, 2015.
22. Gandhir, A. and Y. Hassan, *RANS modeling for flow in nuclear fuel bundle in pressurized water reactors (PWR).* Nuclear Engineering and Design, 2011. **241**(11): p. 4404-4408.
23. Hosokawa, S., et al., *Measurements of turbulent flows in a 2 x 2 rod bundle.* Nuclear Engineering and Design, 2012. **249**: p. 2-13.
24. Xiong, J.B., et al., *Laser Doppler measurement and CFD validation in 3 x 3 bundle flow.* Nuclear Engineering and Design, 2014. **270**: p. 396-403.
25. Holloway, M.V., D.E. Beasley, and M.E. Conner. *Investigation of Swirling Flow in Rod Bundle Subchannels Using Computational Fluid Dynamics*. in *14th International Conference on Nuclear Engineering*. 2006. American Society of Mechanical Engineers.
26. Conner, M.E., E. Baglietto, and A.M. Elmahdi, *CFD methodology and validation for single-phase flow in PWR fuel assemblies.* Nuclear Engineering and Design, 2010. **240**(9): p. 2088-2095.
27. Cinosi, N., et al., *CFD simulation of turbulent flow in a rod bundle with spacer grids (MATIS-H) using STAR-CCM.* Nuclear Engineering and Design, 2014. **279**: p. 37-49.
28. Podila, K. and Y.F. Rao, *CFD modelling of turbulent flows through 5 x 5 fuel rod bundles with spacer-grids.* Annals of Nuclear Energy, 2016. **97**: p. 86-95.
29. Chen, G.L., et al., *Design of a CFD scheme using multiple RANS models for PWR.* Annals of Nuclear Energy, 2017. **102**: p. 349-358.
30. Chen, X., et al., *Validation of CFD analysis for rod bundle flow test with vaned spacer grids.* Annals of Nuclear Energy, 2017. **109**: p. 370-379.
31. Chen, D.Q., et al., *Thermal-hydraulic performance of a 5 x 5 rod bundle with spacer grid in a nuclear reactor.* Applied Thermal Engineering, 2016. **103**: p. 1416-1426.
32. Xiong, J.B., et al., *CFD simulation of swirling flow induced by twist vanes in a rod bundle.* Nuclear Engineering and Design, 2018. **338**: p. 52-62.
33. Koncar, B. and S. Kosmrlj, *Simulation of turbulent flow in MATIS-H rod bundle with split-type mixing vanes.* Nuclear Engineering and Design, 2018. **327**: p. 112-126.
34. Li, X.C. and Y. Gao, *Methods of simulating large-scale rod bundle and application to a 17 x 17 fuel assembly with mixing vane spacer grid.* Nuclear Engineering and Design, 2014. **267**: p. 10-22.
35. Chen, G.L., et al., *CFD simulation for the optimal design and utilization of experiment to research the flow process in PWR.* Annals of Nuclear Energy, 2016. **94**: p. 1-9.
36. Liu, C.C., Y.M. Ferng, and C.K. Shih, *CFD evaluation of turbulence models for flow simulation of the fuel rod bundle with a spacer assembly.* Applied Thermal Engineering, 2012. **40**: p. 389-396.
37. Tseng, Y.S., Y.M. Ferng, and C.H. Lin, *Investigating flow and heat transfer characteristics in a fuel bundle with split-vane pair grids by CFD methodology.* Annals of Nuclear Energy, 2014. **64**: p. 93-99.
38. Liu, C.C. and Y.M. Ferng, *Numerically simulating the thermal-hydraulic characteristics within the fuel rod bundle using CFD methodology.* Nuclear Engineering and Design, 2010. **240**(10): p. 3078-3086.
39. Lifante, C., et al., *3 x 3 rod bundle investigations, CFD single-phase numerical simulations.* Nuclear Engineering and Design, 2014. **279**: p. 60-72.

40. Agbodemegbe, V.Y., et al., *An investigation of the effect of split-type mixing vane on extent of crossflow between subchannels through the fuel rod gaps.* Annals of Nuclear Energy, 2016. **88**: p. 174-185.
41. Ikeda, K., Y. Makino, and M. Hoshi, *Single-phase CFD applicability for estimating fluid hot-spot locations in a 5 x 5 fuel rod bundle.* Nuclear Engineering and Design, 2006. **236**(11): p. 1149-1154.
42. Navarro, M.A. and A.A.C. Santos, *Evaluation of a numeric procedure for flow simulation of a 5 x 5 PWR rod bundle with a mixing vane spacer.* Progress in Nuclear Energy, 2011. **53**(8): p. 1190-1196.
43. Sohag, F.A., L. Mohanta, and F.B. Cheung, *CFD analyses of mixed and forced convection in a heated vertical rod bundle.* Applied Thermal Engineering, 2017. **117**: p. 85-93.
44. Mao, H., et al., *Modeling of spacer grid mixing effects through mixing vane crossflow model in subchannel analysis.* Nuclear Engineering and Design, 2017. **320**: p. 141-152.
45. Lee, J.R., J. Kim, and C.H. Song, *Synthesis of the turbulent mixing in a rod bundle with vaned spacer grids based on the OECD-KAERI CFD benchmark exercise.* Nuclear Engineering and Design, 2014. **279**: p. 3-18.
46. In, W.K., et al., *Numerical computation of heat transfer enhancement of a PWR rod bundle with mixing vane spacers.* Nuclear Technology, 2008. **161**(1): p. 69-79.
47. Miller, D.J., F.B. Cheung, and S.M. Bajorek, *On the development of a grid-enhanced single-phase convective heat transfer correlation.* Nuclear Engineering and Design, 2013. **264**: p. 56-60.
48. Menter, F.R., *2-Equation Eddy-Viscosity Turbulence Models for Engineering Applications.* Aiaa Journal, 1994. **32**(8): p. 1598-1605.
49. Wilcox, D.C., *Reassessment of the Scale-Determining Equation for Advanced Turbulence Models.* Aiaa Journal, 1988. **26**(11): p. 1299-1310.
50. Wallin, S. and A.V. Johansson, *An explicit algebraic Reynolds stress model for incompressible and compressible turbulent flows.* Journal of Fluid Mechanics, 2000. **403**: p. 89-132.
51. Yakhot, V., et al., *Development of Turbulence Models for Shear Flows by a Double Expansion Technique.* Physics of Fluids a-Fluid Dynamics, 1992. **4**(7): p. 1510-1520.
52. Holloway, M.V., et al., *The effect of support grid features on local, single-phase heat transfer measurements in rod bundles.* Journal of Heat Transfer-Transactions of the Asme, 2004. **126**(1): p. 43-53.
53. Acheson, D.J., *Elementary Fluid Dynamics*. 1990, New York: Oxford University Press.
54. Oberlack, M. and H.F. Busse, *Theories of Turbulence*. 2002, New York: Springer-Verlag Wien.
55. Tennekes, H. and J.L. Lumley, *A first course in Turbulence*. 1972, England The MIT Press